New Insights into Inhibitor Design from the Crystal Structure and NMR Studies of *Escherichia coli* GAR Transformylase in Complex with β-GAR and 10-Formyl-5,8,10-trideazafolic Acid[†,‡]

Samantha E. Greasley,[§] Mason M. Yamashita,[§,||] Hui Cai,[§] Stephen J. Benkovic,[⊥] Dale L. Boger,[§] and Ian A. Wilson*[,§]

Departments of Molecular Biology and Chemistry and The Skaggs Institute for Chemical Biology, The Scripps Research Institute, 10550 North Torrey Pines Road, La Jolla, California 92037, and Department of Chemistry, Pennsylvania State University, University Park, Pennsylvania 16802

Received August 12, 1999; Revised Manuscript Received October 18, 1999

ABSTRACT: The crystal structure of *Escherichia coli* GAR Tfase at 2.1 Å resolution in complex with 10-formyl-5,8,10-trideazafolic acid (10-formyl-TDAF, K_i = 260 nM), an inhibitor designed to form an enzyme-assembled multisubstrate adduct with the substrate, β-GAR, was studied to determine the exact nature of its inhibitory properties. Rather than forming the expected covalent adduct, the folate inhibitor binds as the hydrated aldehyde (gem-diol) in the enzyme active site, in a manner that mimics the tetrahedral intermediate of the formyl transfer reaction. In this hydrated form, the inhibitor not only provides unexpected insights into the catalytic mechanism but also explains the 10-fold difference in inhibitor potency between 10-formyl-TDAF and the corresponding alcohol, and a further 10-fold difference for inhibitors that lack the alcohol. The presence of the hydrated aldehyde was confirmed in solution by $^{13}C-^{1}H$ NMR spectroscopy of the ternary GAR Tfase−β-GAR−10-formyl-TDAF complex using the ^{13}C-labeled 10-formyl-TDAF. This insight into the behavior of the inhibitor, which is analogous to protease or transaminase inhibitors, provides a novel and previously unrecognized basis for the design of more potent inhibitors of the folate-dependent formyl transfer enzymes of the purine biosynthetic pathway and development of anti-neoplastic agents.

Glycinamide ribonucleotide transformylase (GAR Tfase)[1] catalyzes the first of two steps in the de novo purine biosynthesis pathway that requires folate cofactors (*1*−*3*). The transfer of a formyl group from 10-formyl-tetrahydrofolate (10-formyl-THF) to the primary amine of β-glycinamide ribonucleotide (β-GAR) introduces C8 into the purine ring (Figure 1). GAR Tfase, like dihydrofolate reductase (DHFR, folate metabolism) (*4*, *5*) and thymidylate synthase (TS, pyrimidine biosynthesis) (*6*, *7*), is now established as an important target for anti-neoplastic intervention (*8*, *9*).

The tetrahydrofolate analogue, (6*R*,6*S*)-5,10-dideaza-5,6,7,8-tetrahydrofolic acid (DDATHF, Figure 2), is a potent and selective inhibitor of GAR Tfase and exhibits effective activity in vitro against solid murine and human tumors where methotrexate, a potent dihydrofolate reductase inhibitor, has little or no effect (*10*, *11*). The selectivity of DDATHF is attributed to the fact that tumor cells rely heavily on de novo purine synthesis while, in most normal tissues, the salvage pathway is the primary source for purine supply (*12*). The (6*R*)-diastereomer, lometrexol (LTX, K_i = 60 nM), is presently in clinical trials due to its effective antitumor activity and reduced general cytotoxicity, when co-administered with folic acid (*13*).

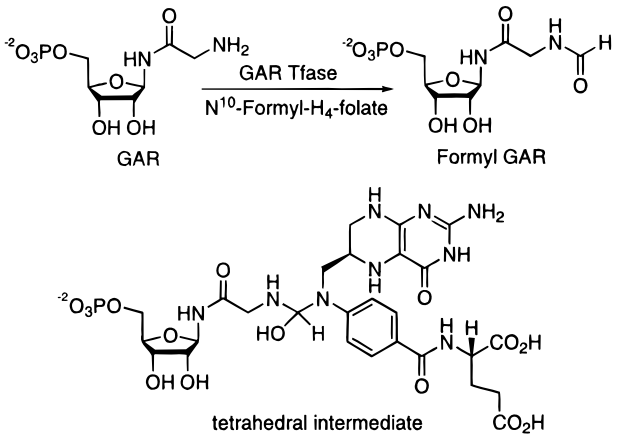

FIGURE 1: Formyl transfer reaction catalyzed by GAR Tfase, with the proposed tetrahedral intermediate.

† This work was supported by NIH Grant CA63536 to I.A.W., D.L.B., and S.J.B.

‡ The coordinates for the (10*S*)- and (10*R*)-inhibitor structures have been deposited with the Protein Data Bank under file names 1C2T and 1C3E, respectively.

* To whom correspondence should be addressed. E-mail: wilson@scripps.edu. Phone: (858) 784-9706. Fax: (858) 784-2980.

§ The Scripps Research Institute.

|| Present address: Signal Pharmaceuticals Inc., 5555 Oberun Dr., San Diego, CA 92121.

⊥ Pennsylvania State University.

[1] Abbreviations: GAR Tfase, glycinamide ribonucleotide transformylase; 10-formyl-TDAF, 10-formyl-5,8,10-trideazafolic acid; 10-formyl-THF, 10-formyl-tetrahydrofolate; DHFR, dihydrofolate reductase; TS, thymidylate synthase; DDATHF, (6*R*,6*S*)-5,10-dideaza-5,6,7,8-tetrahydrofolic acid; MPD, methylpentanediol; NMR, nuclear magnetic resonance.

10.1021/bi991888a CCC: $18.00
Published on Web 11/25/1999

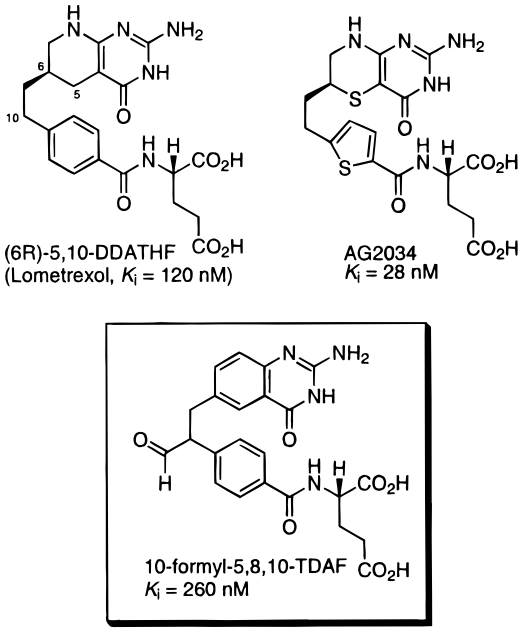

FIGURE 2: Representatives of GAR Tfase inhibitors.

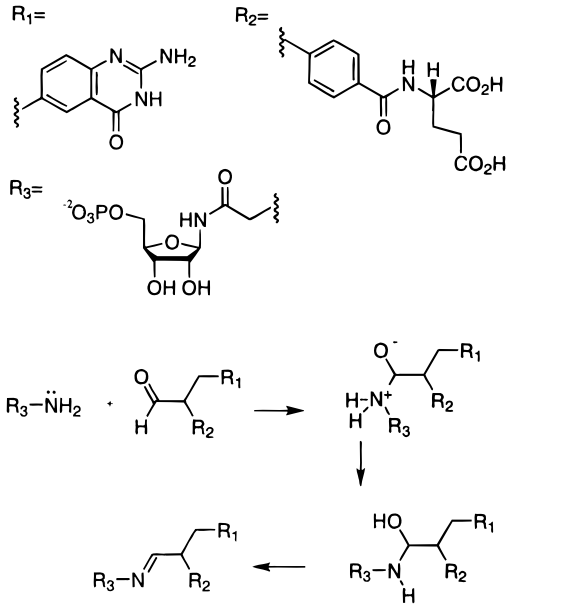

FIGURE 3: Mechanism of imine bond formation. Nucleophilic addition by attack from the primary amine of β-GAR (R_3) to the aldehyde of 10-formyl-TDAF, followed by rapid proton transfer, results in the unstable carbinolamine. A proton associates with the hydroxyl group forming a protonated hemiaminal followed by elimination of water. The final step involves the loss of a proton from the imine nitrogen.

More recently, a number of antifolates specific to GAR Tfase have been identified. Habeck et al. (*14*) described the development of two promising selective GAR Tfase inhibitors based on the DDATHF core, where the *p*-aminobenzoic acid moiety is replaced by a 2′,5′-thiophene (LY254155, K_i = 2.1 nM) and a 2′,5′-furan (LY222306, K_i = 0.77 nM). Boritzki et al. (*15*) described the synthesis and characterization of AG2034 (K_i = 28 nM), a close relative to LY254155, that enlists a 5-thia-DDATHF core system (Figure 2). All of these inhibitors show specific, low nanomolar inhibition of GAR Tfase and in vivo antitumor activity, and are presently being evaluated for potential clinical use (*16*).

In parallel to these studies, the focus of our work has been to utilize the knowledge obtained from various X-ray structures of GAR Tfase (*17*−*20*) to design a novel compound capable of forming an enzyme-assembled, tight binding inhibitor specific to GAR Tfase. The inhibitor 10-formyl-5,8,10-trideazafolic acid (10-formyl-TDAF, Figure 2) was designed to form a covalent imine bond with the substrate, β-GAR, within the active site by replacement of N10 with a carbon, which would prevent breakdown of the tetrahedral intermediate via a formyl transfer reaction (Figure 3) (*21*). However, should the imine bond not form, competitive inhibition, which is selective for GAR Tfase over other folate-dependent enzymes not involved in a formyl transfer reaction, would still be expected to be observed. The design of 10-formyl-TDAF also takes advantage of the replacement of the sensitive pterin core of the natural folate cofactor with a quinazoline, which has been shown to be an effective cofactor substitute for GAR Tfase (*22*).

Boger et al. (*21*) reported the synthesis and characterization of 10-formyl-TDAF which demonstrated competitive inhibition of GAR Tfase with a K_i of 260 nM, comparable to the (6*R*,6*S*)-mixture of DDATHF. 10-Formyl-TDAF proved to be an effective inhibitor of GAR Tfase, binding approximately 100 times more effectively than the cofactor 10-formyl-5,8-dideazafolic acid (K_i = 17 μM), and being 12 times more potent than the corresponding alcohol (K_i = 3.1 μM) (*23*) and approximately 100 times more potent than other C10-substituted TDAFs possessing either an sp^3 or sp^2 C10 center (*23*, *24*). In addition, the inhibitor is 10 times more potent than a simplified multisubstrate adduct inhibitor based on the TDAF core (*25*), and 10−100 times more potent than the most effective N10-substituted 5,8-dideazafolic acid derivatives (*26*, *27*). The 10-formyl-TDAF exists exclusively in the hemiacetal form in methanol and readily forms an imine upon treatment with glycinamide (*21*). The effect of the nontransferable aldehyde was found to be general and enhanced the potency of other related analogues against GAR Tfase (*21*, *28*). Despite these properties, 10-formyl-TDAF displayed simple competitive inhibition of GAR Tfase and did not exhibit the expected tight binding or time-dependent inhibition, characteristic of formation of an enzyme-assembled multisubstrate adduct inhibitor. Furthermore, the K_i is 2−3 orders of magnitude higher than those of typical multisubstrate adduct inhibitors [for example, TGDDF (K_i = 250 pM) and BW1476U89 (K_i = 100 pM) (*29*)].

A number of possible explanations could account for this nature of the inhibition of GAR Tfase by this compound. A rapid, yet readily reversible, imine bond may be formed with β-GAR which provides some enhancement of binding affinity, but without formation of a stable multisubstrate adduct. Alternatively, the carbonyl oxygen of the aldehyde may form hydrogen bonds with active site residues, such as residues Asn 106 or His 108, thereby enhancing the binding affinity. A third possibility is that the aldehyde may react with an active site nucleophile to form a reversible hemiacetal type adduct.

The X-ray crystal structure of *Escherichia coli* GAR Tfase in complex with 10-formyl-5,8,10-trideazafolic acid and β-GAR was determined to 2.1 Å resolution to address the origin of the inhibitory properties of 10-formyl-TDAF and to establish whether the multisubstrate adduct is indeed formed. An NMR spectroscopic study was subsequently

performed with a ^{13}C-labeled inhibitor to test and unambiguously confirm the hypothesis that emerged from analysis of the crystal structure that the 10-formyl-TDAF ligand bound in the hydrated state.

MATERIALS AND METHODS

Materials. Luria broth and agar were obtained from Life Technologies (Gaithersburg, MD). All common buffers and reagents were purchased from Sigma-Aldrich Corp. (St. Louis, MO).

Protein Preparation. E. coli GAR Tfase was prepared as described by Inglese et al. (*3*). Cells were grown in LB medium with 100 μg/mL ampicillin at 37 °C to an OD of 0.6, induced with 1.0 μM IPTG, and grown for an additional 8 h. Cells were harvested by centrifugation and resuspended in a minimal volume of 50 mM Tris-HCl (pH 7.5), 50 mM NaCl, 1 mM EDTA, and protease inhibitors (buffer A).

Protein Purification. Lysozyme (1 mg/mL) was added to the cell suspension; cells were disrupted by sonication, and the lysate was clarified by centrifugation at 20000*g* for 60 min. Supernatant was dialyzed against 4 L of buffer A overnight at 4 °C. The dialyzed material was loaded onto a 50 mL DE-52 anion exchange column and eluted with a 0 to 3 M NaCl gradient. Eluted fractions containing GAR Tfase protein were detected by SDS−PAGE, pooled, concentrated, and loaded onto a 500 mL Superdex 200 high-resolution gel filtration column (Pharmacia Biotech Inc., Piscataway, NJ), equilibrated with 50 mM Tris-HCl and 50 mM NaCl (pH 7.5). Fractions containing GAR Tfase, based on SDS−PAGE analysis, were again pooled and concentrated to 20 mg/mL using Millipore Ultrafree-15 devices. Approximately 25 mg of GAR Tfase is obtained from a 1 L preparation of cells and is 98% pure, as assessed by SDS−PAGE.

Crystallization and Data Collection. Crystals of *E. coli* GAR Tfase in complex with β-GAR and 10-formyl-TDAF were grown by the method of vapor diffusion in sitting drops (*30*). A protein solution at a concentration of 20 mg/mL containing a 10-fold molar excess of both inhibitor and (α,β)-GAR were mixed with an equal volume (1.8 μL) of a precipitating solution of 18% polyethylene glycol 3350 (v/v), 0.1 M imidazole malate (pH 7.2), 0.15 M calcium chloride, and 4% MPD (v/v). The sitting drop trays were equilibrated at 22 °C, and precipitate was observed in the drops 24 h after being set up. Crystals grew out of this precipitate after 3−7 days. The crystals had a morphology of thin plates, with maximum dimensions of 0.2 mm × 0.1 mm × 0.05 mm, and were typically multilayered and difficult to separate.

After many crystals had been screened, a complete data set was collected from a single cryoprotected crystal at −179 °C on beam line 9-1 at Stanford Synchrotron Radiation Laboratory with a wavelength of 0.98 Å. The crystal was mounted in a loop (Hampton Research, Laguna Hills, CA) and transferred quickly through a cryosolution of 10% MPD in mother liquor before being flash-cooled in the liquid nitrogen stream (*31*). Data were collected on a MAR345 Research imaging plate, with a crystal-to-detector distance of 170 mm, a plate diameter of 180 mm, and an oscillation angle of 2.0°. The HKL V1.9.1 package (*32*) was used to process and scale the data to 2.1 Å resolution. The crystal space group is $P2_1$ with the following unit cell dimensions: a = 40.3 Å, b = 112.8 Å, c = 47.0 Å, and β = 101.6° (Table 1). Calculation of the Matthews coefficient (V_m = 2.3) (*33*) suggests two molecules per asymmetric unit with a solvent content of 45.4%.

Table 1: Data Collection Statistics

space group	$P2_1$
unit cell dimensions	a = 40.3 Å, b = 112.8 Å, c = 47.0 Å, β = 101.6°
no. of molecules per au	2
resolution range (Å)	20−2.1 (2.17−2.1)[a]
no. of unique reflections	23742 (2338)
completeness (%)	99.2 (99.3)
multiplicity	2.9 (2.8)
average I/σ	13.0 (1.9)
R_{merge}[b] (%)	8.3 (42.1)

[a] Numbers in brackets refer to the highest-resolution shell. [b] $R_{merge} = [\Sigma_h\Sigma_i|I_i(h) - \langle I(h)\rangle|/\Sigma_h\Sigma_i I_i(h)] \times 100$, where $\langle I(h)\rangle$ is the mean of the $I(h)$ observation of reflection h.

Structure Solution and Refinement. The structure was determined by the method of molecular replacement using the program AMoRe from the CCP4 package (*34*, *35*). The search model used was monomer 1 from the 1.96 Å structure of Klein et al. (PBD file 1GAR) (*19*) and included residues 1−121 and 127−209. The rotation search from 10.0 to 3.5 Å revealed two strong solutions with peak heights of 34.3σ and 32.3σ (the next highest peak was 14.4σ). The translation function gave a clear solution for each molecule that, after the rigid body fitting step in AMoRe, resulted in an R value of 38.7% with a correlation coefficient of 68.7%. The crystal packing showed that this crystal form does not exhibit the intimate dimer observed in previous structures at low pH (*17*−*19*).

Structure refinement and electron density map calculations were initially performed using X-PLOR version 3.851 (*36*) with a 5% test set (917 reflections) of data set aside for R_{free} cross validation (*37*). Rigid body refinement in the resolution range from 10 to 3.5 Å gave an R_{free} and an R_{cryst} of 41.3 and 45.3%, respectively. Electron density maps at this stage provided clear evidence for the position of the inhibitor, 10-formyl-TDAF, but weaker density for the substrate β-GAR in both monomers. Cycles of manual rebuilding with O (*38*) were alternated with conventional positional refinement or simulated annealing and individual B-value refinement with X-PLOR using data from 20.0 to 2.1 Å with a 2σ cutoff on F_o. Electron density maps (σ_A-weighted $2F_o - F_c$ and $F_o - F_c$) were calculated after each cycle of refinement in addition to simulated annealing and shake omit maps for poorly defined regions of the structure. The residues that required the most rebuilding were 110−131, which adopt the loop−helix conformation observed in the other high-pH GAR Tfase structures (*18*, *20*), and the flexible loop of residues 141−146. After the first round of positional refinement, the inhibitor and the β-anomer of the substrate, GAR, were included in the model. The glycine moiety of the β-GAR still had weak density, but the well-defined electron density around the anomeric carbon (C1) of GAR gave no indication of additional binding of the α-anomer. This interpretation is in agreement with kinetic studies that show only β-GAR is utilized by GAR Tfase and that the presence of α-GAR in the anomeric mixture has no effect on enzyme activity (*39*, *40*). InsightII (MSI, San Diego, CA) was used to generate and minimize coordinates for 10-formyl-TDAF, and the

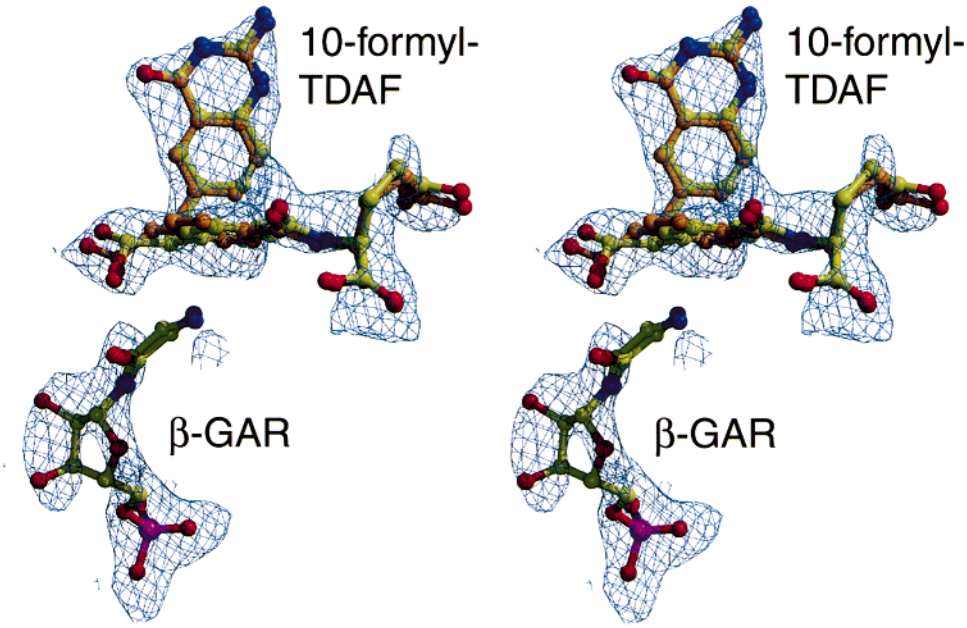

FIGURE 4: Stereoview of the electron density and coordinates for hydrated forms of 10-formyl-TDAF and β-GAR for molecule 1 illustrating how both the (10*R*)- (orange) and (10*S*)-hydrated (yellow) forms of the inhibitor may be modeled. The density shown is from a $3F_o - 2F_c$ σ_A-weighted map contoured at 1σ.

topology and parameter files required by X-PLOR were generated by XPLO2D (*41*). Coordinates and X-PLOR files for β-GAR were extracted from the Hetero-Compound Information Centre-Uppsala (HIC-UP, Uppsala, Sweden). During later rounds of refinement, the parameter files for both inhibitor and substrate were optimized by hand and the geometry of the structures was assessed by comparison to similar structures in the Cambridge Structural Database. The electron density around the formyl transfer region suggests that both the (10*R*)- and (10*S*)-diastereomers can bind in the active site. In addition, the density provides evidence that the (10*R*,10*S*)-10-formyl-TDAF is present as the hydrated aldehyde (Figure 4). In an attempt to determine which form of the inhibitor is bound, refinement was carried out with the (10*R*)- and (10*S*)-forms and the hydrated (10*R*)- and (10*S*)-forms of the inhibitor separately. The resulting R_{free} and R_{cryst} values were similar for each form of the inhibitor; however, the density favored the hydrated (10*R*,10*S*)-10-formyl-TDAF. Following the unequivocal results of the NMR studies, only the hydrated aldehyde forms of the inhibitor were refined.

Noncrystallographic symmetry (NCS) restraints were applied throughout refinement. The initial restraints of 200 and 100 kcal mol^{-1} Å^2 for main chain and side chain atoms, respectively, were reduced in the final rounds of refinement to 100 for main chain atoms and 50 for side chain atoms, but were not released completely. The final rmsd between molecule 1 and molecule 2 is 0.14 Å for Cα atoms and 0.48 Å for all protein atoms. In addition to NCS restraints, an overall anisotropic temperature factor correction (where $B_{11} = -7.6$ Å^2, $B_{22} = 10.8$ Å^2, $B_{33} = -3.3$ Å^2, $B_{12} = B_{23} = 0.0$ Å^2, and $B_{13} = 4.0$ Å^2) was applied, in addition to a bulk solvent correction (*42*). Water molecules were added during the final stages of refinement using the water picking routine in X-PLOR. After each round of refinement, all water molecules were examined, and those with *B*-values greater than twice the average *B*-value for the protein were discarded, along with water molecules without good hydrogen bonds to the protein. After refinement in X-PLOR, the R_{free} and R_{cryst} in the resolution range of 20−2.1 Å, with a 2σ cutoff on F_o, were 28.7 and 21.7%, respectively, for the (10*S*)-hydrated aldehyde and 28.8 and 21.3%, respectively, for the (10*R*)-hydrated aldehyde. A further two cycles of model building and refinement were performed using the CNS version 0.3 (*43*), with the maximum likelihood target. The subsequent electron density maps for all regions of the structure were improved over the X-PLOR maps, and minimal remodeling of the structure was required. The final R_{free} and R_{cryst} for the model refined with the (10*S*)-hydrated aldehyde form of the inhibitor are 26.5 and 22.7% and for the (10*R*)-hydrated aldehyde 26.3 and 22.7%, respectively. A summary of the refinement statistics is given in Table 2 along with the geometry of the model, as analyzed by PROCHECK (*44*).

Table 2: Refinement Statistics for GAR Tfase for Both of the Hydrated Forms, (10*R*)- and (10*S*)-Formyl-TDAF, and β-GAR

resolution range (Å)	20−2.1
data cutoff	$F_o > 2\sigma$
no. of reflections (test set)	18883 (917)
no. of protein atoms	3236
no. of water molecules	197
no. of inhibitor atoms	70
no. of substrate atoms	36
R_{cryst}[a] (%) (*R*, *S*)	22.7, 22.7
R_{free}[a] (%) (*R*, *S*)	26.3, 26.5
rmsd for bond lengths (Å)	0.011
rmsd for bond angles (deg)	1.55
Ramachandran plot (%)	
favored	89.8
allowed	9.9
generously allowed	0.3
disallowed	0.0

[a] $R_{cryst} = (\Sigma_h|F_o - F_c|/\Sigma_h F_o) \times 100$, where F_o and F_c are the observed and calculated structure factor, respectively. R_{free} is computed as described for R_{cryst}, but with the test set of reflections only.

Scheme 1

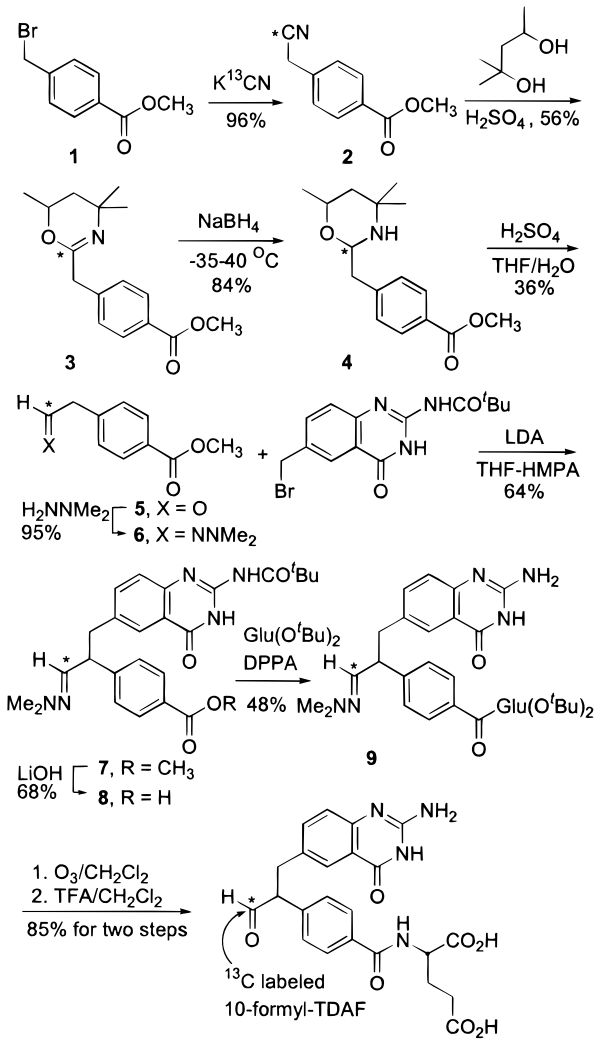

Preparation of [13C-Labeled 10-Formyl-5,8,10-trideazafolic Acid ([13C]-10-Formyl-TDAF): Methyl 4-([13C]Cyanomethyl)benzoate (2). A solution of methyl 4-(bromomethyl)-benzoate (Scheme 1, **1**, 1.0 g, 4.37 mmol) in 1,4-dioxane (15 mL) and H_2O (6.5 mL) was treated with $K^{13}CN$ (99% enriched, 341 mg, 5.24 mmol, 1.2 equiv). The reaction mixture was stirred at 25 °C for 36 h before the addition of H_2O (10 mL) and extraction with EtOAc (3 × 15 mL). The organic layers were combined and concentrated to afford **2** (1.47 g, 96%) as a white crystalline solid: $R_f = 0.35$ (20% EtOAc/hexane); mp 49−51 °C; ^{1}H NMR ($CDCl_3$, 400 MHz) δ 8.05 (d, $J = 8.3$ Hz, 2H), 7.41 (d, $J = 8.4$ Hz, 2H), 3.92 (s, 3H), 3.79 (d, $J = 10.7$ Hz, 2H); ^{13}C NMR ($CDCl_3$, 100 MHz) δ 117.2; IR (neat) υ_{max} 2954, 2195, 1712, 1615, 1431, 1404, 1286, 1192, 1113, 742 cm^{-1}; FAB-HRMS (NBA) *m/z* 177.0737 (M + H$^+$, $C_9{}^{13}C_1H_9NO_2$ 177.0745).

Methyl 4-(5,6-Dihydro-4,4,6-trimethyl-4H-1,3-oxazin-2-yl)-2-[13C]methylbenzoate (3). A solution of **2** (3.36 g, 19 mmol, 1.1 equiv) in CH_2Cl_2 (2.5 mL) was cooled to 0 °C and slowly treated with concentrated H_2SO_4 (3.5 mL) followed by 2-methyl-2,4-pentanediol (2.22 mL, 17.4 mmol). The reaction mixture was allowed to stir at 0 °C for an additional 80 min and poured into ice water (ca. 100 g). The aqueous solution was extracted with CH_2Cl_2 (3 × 30 mL). Flash column chromatography (20% EtOAc/hexane) of the concentrated organic extracts provided the recovered starting material in 20% yield. The aqueous solution was basified with addition of solid $NaHCO_3$ and extracted with EtOAc (3 × 50 mL). The combined organic layers were washed with H_2O, saturated aqueous NaCl, dried over Na_2SO_4, and concentrated to provide **3** (2.96 g, 56%) as a light orange-yellow solid: $R_f = 0.30$ (50% EtOAc/hexane); mp 46−48 °C; ^{1}H NMR ($CDCl_3$, 400 MHz) δ 7.94 (d, $J = 8.2$ Hz, 2H), 7.35 (d, $J = 8.4$ Hz, 2H), 4.12−4.03 (m, 1H), 3.88 (s, 3H), 3.48 (d, $J = 7.5$ Hz, 2H), 1.69 (dd, $J = 13.6$, 2.7 Hz, 1H), 1.38−1.05 (m, 10H); ^{13}C NMR ($CDCl_3$, 100 MHz) δ 156.3; IR (neat) υ_{max} 2965, 1721, 1629, 1604, 1434, 1277, 1253, 1180, 1102, 1043, 760 cm^{-1}; FAB-HRMS (NBA/NaI) *m/z* 277.1630 (M + H$^+$, $C_{15}{}^{13}C_1H_{21}NO_3$ 277.1633).

Methyl 4-(Tetrahydro-4,4,6-trimethyl-2H-1,3-oxazin-2-yl)-2-[13C]methylbenzoate (4). A solution of $NaBH_4$ was prepared by dissolving $NaBH_4$ (138 mg, 1 equiv) in a minimum amount of H_2O (ca. 150−200 μL) in which NaOH (40%, 2 μL) was present. The $NaBH_4$ solution and a 9 N HCl solution were introduced alternately at −35 to −40 °C to a 100 mL beaker charged with **3** (1.0 g, 3.64 mmol) in a solvent mixture of THF (3.64 mL) and ethanol (95%, 3.64 mL) such that a pH 6−8 was maintained. After addition of the $NaBH_4$ solution, the reaction mixture was stirred at −35 to −40 °C for an additional 1 h with the occasional addition of the HCl solution to maintain a pH of 6−8. The reaction mixture was then poured into ice water (20 mL), basified with addition of saturated aqueous $NaHCO_3$, and extracted with EtOAc (3 × 20 mL). The combined organic layers were washed with H_2O and saturated aqueous NaCl, dried over Na_2SO_4, and concentrated. Flash column chromatography (SiO_2, 30% EtOAc/hexane) provided **4** (0.84 g, 84%) as a light yellow crystalline solid: $R_f = 0.35$ (50% EtOAc/hexane); mp 69−71 °C; ^{1}H NMR ($CDCl_3$, 400 MHz) δ 7.94 (d, $J = 8.2$ Hz, 2H), 7.35 (d, $J = 8.2$ Hz, 2H), 4.46 (dt, $J = 15.2$, 4.6 Hz, 1H), 3.89 (s, 3H), 3.73−3.69 (m, 1H), 2.92−2.87 (m, 2H), 1.39 (dd, $J = 13.2$, 2.2 Hz, 1H), 1.13−0.91 (m, 11H); ^{13}C NMR ($CDCl_3$, 100 MHz) δ 83.0; IR (neat) υ_{max} 2965, 1721, 1609, 1434, 1277, 1180, 1102, 990, 765 cm^{-1}; FAB-HRMS (NBA/NaI) *m/z* 279.1787 (M + H$^+$, $C_{15}{}^{13}C_1H_{23}NO_3$ 279.1790).

[1-13C]-4-(Methoxycarbonyl)phenylacetaldehyde (5). A solution of **4** (100 mg, 0.36 mmol) in THF (2 mL) and H_2O (0.3 mL) was treated with 4 M aqueous H_2SO_4 (54.2 μL) at 0 °C, and the reaction mixture was warmed to 80 °C and stirred for 3 h. The reaction mixture was quenched with the addition of EtOAc (2 mL) and saturated aqueous $NaHCO_3$ (0.5 mL). The organic layer was washed with H_2O and saturated aqueous NaCl, dried over Na_2SO_4, and concentrated. Flash column chromatography (SiO_2, 5 to 20% EtOAc/hexane gradient elution) provided **5** (23 mg, 36%) as a light yellow thick oil identical in all respects to authentic material (*21*): ^{13}C NMR ($CDCl_3$, 100 MHz) δ 198.3.

Methyl [2-13C]-4-(2-Dimethylhydrazonoethyl)benzoate (6). This was prepared as described by Boger et al. (*21*): ^{13}C NMR ($CDCl_3$, 100 MHz) δ 135.1.

Methyl (2R)-4-[1-Dimethylhydrazono[13C]-3-(2-trimethylacetimido-3,4-dihydro-4-oxo-quinazolin-6-yl)prop-2-yl]benzoate (7)*. This was prepared as described by Boger et al. (*21*): ^{13}C NMR ($CDCl_3$, 100 MHz) δ 137.0.

(2R)-4-[3-(2-Amino-3,4-dihydro-4-oxoquinazolin-6-yl)-1-(dimethylhydrazono)prop-2-yl]benzoic Acid (8)*. This was prepared as described by Boger et al. (*21*): ^{13}C NMR (DMF-d_7, 100 MHz) δ 139.4.

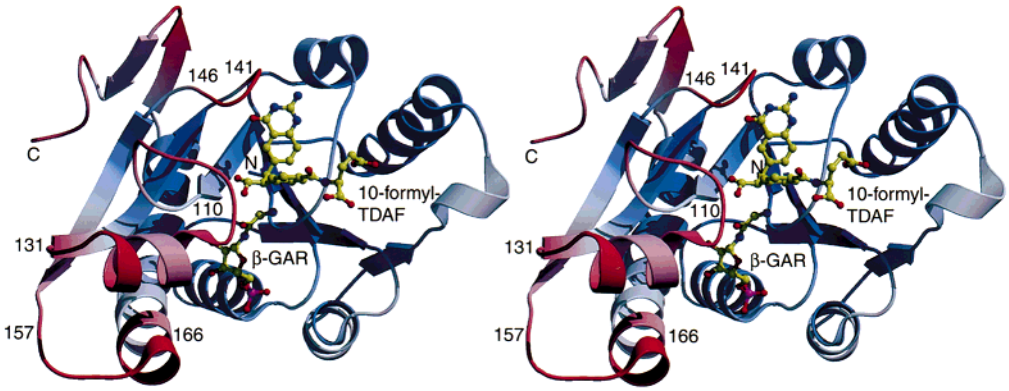

FIGURE 5: Stereo representation of the structure of *E. coli* GAR Tfase showing the position of the bound hydrated form of the inhibitor, 10-formyl-TDAF, and substrate, β-GAR. The figure is colored by *B*-values with a gradient ranging from low (10 Å^2, blue) to high (55 Å^2, red), which illustrate the more disordered regions of the structure (red).

Di-tert-butyl (2RS)-N-{4-[(2-Amino-3,4-dihydro-4-oxoquinazolin-6-yl)-1-(dimethylhydrazono)[^{13}C]propyl-2-yl]benzoyl}-L-*glutamate* (**9**). This was prepared as described by Boger et al. (*21*): ^{13}C NMR (DMSO-d_6, 100 MHz) δ 141.7, 140.8.

(10RS)-10-Formyl[^{13}C]-5,8,10-trideazafolic Acid (10-Formyl[^{13}C]TDAF). A solution of **9** (5.0 mg, 8.1 μmol) in CH_2Cl_2 (1 mL) was cooled to −78 °C and treated with ozone until the solution became very light blue. The solvent and excess ozone were removed under a stream of nitrogen, followed by addition of a solution of trifluoroacetic acid (40 μL) in CH_2Cl_2 (120 μL) at 0 °C. The reaction mixture was stirred at 0 °C for 2 h and at 25 °C for 12 h. Et_2O (1 mL) was added to the reaction mixture to precipitate the product (3.2 mg, 85% for two steps) which was identical in all respects with the authentic material (*21*): ^{13}C NMR (DMSO-d_6, 100 MHz) δ 200.7, 200.6.

NMR Spectroscopy of the ^{13}C-Labeled Inhibitor, the Enzyme−Inhibitor Complex, and the Substrate−Enzyme−Inhibitor Complex. All NMR experiments were performed on a Bruker DRX-600 NMR spectrometer at 25 °C. ^{1}H−^{13}C heteronuclear multiple-quantum coherence spectra [HMQC (*45*)] using gradient pulse with coherence selection step after t_1 were obtained in D_2O with ^{13}C decoupling during acquisition. For each FID, 12 transients were acquired over 2048 data points. A total of 256 FIDs were obtained in the t_1 dimension for each data set. The ^{1}H and ^{13}C sweep widths were set to 12 and 230 ppm, respectively. Final FIDs were weighed with a Guassian function on the f_2 dimension and a 90° shifted sine-bell-squared function on the f_1 dimension, and zero-filled to obtain a 4096 × 512 data matrix. All HMQC spectra were recorded at pD 7.5 (20 mM sodium phosphate/1 mM EDTA, D_2O) with DMSO added as an internal standard.

RESULTS AND DISCUSSION

X-ray Structure Determination. The structure of *E. coli* GAR Tfase, cocrystallized with (10*R*,10*S*)-10-formyl-TDAF and (α,β)-GAR, was determined to 2.1 Å resolution (Table 1) by molecular replacement; monomer 1 of the 1.96 Å structure of Klein et al. (PDB file 1GAR) (*19*) was used as the search model. The complex was crystallized at pH 7.2 from polyethylene glycol (PEG 3350) with two molecules in the asymmetric unit (see methods), but does not exhibit the intimate dimer observed in phosphate-bound and complex GAR Tfase structures at low pH (5.5−6.75) (*17*−*19*). The final model of both molecules 1 and 2 contains all residues except for the C-terminal residues (210−212), for which there is no convincing electron density, as observed in previous structures (*17*−*20*). The β-anomer of the substrate, β-GAR, and both the (10*R*)- and (10*S*)-diastereomers of the inhibitor are present in each monomer. The refinement statistics and structure analysis are presented in Table 2.

Table 3: Comparison of *B*-Values for *E. coli* GAR Tfase 10-Formyl-TDAF−β-GAR and 5,8-DDATHF−β-GAR Complex Structures for Disordered Regions, the Inhibitor, and the Substrate, β-GAR

	10-formyl-TDAF−β-GAR		5,8-DDATHF−β-GAR (Å^2)[c]
structure	molecule 1 (Å^2)	molecule 2 (Å^2)	
all protein atoms	28.2	31.0	24.8
inhibitor[a]	39.9 (*R*), 41.4 (*S*) (1.4 for *R*, 1.5 for *S*)[b]	46.3 (*R*), 46.5 (*S*) (1.5 for *R*, 1.5 for *S*)	56.0 (2.3)
β-GAR	54.7 (1.9)	60.1 (1.9)	25.8 (1.0)
residues 110−131	41.2 (1.5)	41.0 (1.3)	46.5 (1.4)
residues 141−146	47.7 (1.7)	43.0 (1.4)	46.3 (1.9)
residues 157−166	44.3 (1.6)	37.4 (1.2)	49.2 (2.0)

[a] *R* and *S* refer to the (10*R*)- and (10*S*)-diastereomers of the hydrated aldehyde form of 10-formyl-TDAF, both of which are modeled in the structure. [b] The numbers in parentheses are the ratio of the protein segment or ligand *B*-value to that of the overall protein (residues 1−209). [c] PDB file 1CDE (*18*).

Overall Structure. The overall topology of the protein is identical to those of previously published structures (Figure 5), with the closest similarity [rmsd of 1.16 Å (molecule 1) and 1.13 Å (molecule 2) for all protein atoms] being to the 5-deazatetrahydrofolate (5-DATHF)−β-GAR complex (*18*). Analysis of the *B*-values reveals three regions of high thermal mobility, in agreement with all GAR Tfase structures determined to date (*20*) (Figure 5). These regions include the flexible pH-dependent loop−helix region of residues 110−131, the active site loop of residues 141−146 containing Asp 144 (*46*), and a third loop of residues 157−166 (Table 3). Indeed, residues 110−131 adopt the loop−helix conformation observed in the 5-DATHF−β-GAR ternary complex (*18*) and the pH 7.5 mutant monomeric Glu 70 Ala GAR Tfase structure (*20*), presumably due to the stabilization derived from physiologic pHs (*20*). This ordered loop−helix conformation provides not only a hydrophobic lid to the

cofactor and substrate binding pocket but also two main chain hydrogen bonds to catalytic residues His 108 and Asp 144, thus preparing the active site for catalysis (*20*). The electron density for the loop containing residues 141−146 is particularly weak. A comparison of the conformations of this loop in the available crystal structures reveals that it adopts a wide range of conformations from occupying the folate binding pocket, to a more open conformation when folates are bound, to a completely extended conformation where Asp 144 is no longer in the active site (*20*). As discussed previously (*20*), the loop conformation may be affected by crystal packing interactions. However, the range of discrete conformations may mimic the structural snapshots of events in the formyl transfer reaction where, upon folate binding, the loop moves to a conformation that positions Asp 144 adjacent to His 108 in a salt bridge interaction that promotes the stabilization of the positive charge on the imidazolium (*20*). Upon completion of the formyl-carbon transfer reaction, the loop of residues 141−146 may need to flip out of the active site to facilitate cofactor release. The movement observed for this loop may, therefore, account for the conformational isomerization that is evident from the kinetic data (*47*). Despite the weak electron density for the loop of residues 141−146, its conformation is similar to that observed for the multisubstrate adduct inhibitor BW1476U89 and the 5-DATHF−β-GAR complex structures. This "folate-bound" position is stabilized by a hydrogen bond from the backbone amide group of Gly 117 (loop of residues 110−131) to the side chain carboxylate of Asp 144, hydrogen bonds from the backbone of Thr 140 and Asp 144 to the quinazoline of 10-formyl-TDAF, and a salt bridge from Asp 144 to His 108.

Ligand Binding Site. The electron density for 10-formyl-TDAF clearly reveals that the inhibitor is bound in the 20 Å long active site binding pocket in a location similar to that observed for the folate portions of the BW1476U89 multisubstrate adduct inhibitor complex (*19*) and the 5-DATHF−β-GAR ternary complex (*18*). The electron density around the formyl region suggests that both the (10*R*)- and (10*S*)-diastereomer forms of the inhibitor may be bound. The quinazoline, *p*-aminobenzoic acid, and glutamate portions of the two diastereomers occupy similar positions (Figure 4). The quinazoline ring is located in the pteridine binding site, and overlaps with the pyrimidone ring of the inhibitor BW1476U89 (*19*). The inhibitor is surrounded by a number of hydrophobic residues, including Leu 85, Phe 88, Leu 92, Phe 96, Val 97, Leu 104, and Val 139. All of the hydrophilic interactions are derived from main chain contacts, including residues from the flexible loop of residues 141−146 (Table 4). Replacement of N8 of the natural cofactor with carbon results in the loss of a hydrogen bond to the main chain carbonyl of Arg 90.

The benzoyl ring of the *p*-aminobenzoic acid has been modeled in one conformation, but appears to exhibit some degree of rotational flexibility, as was observed in the BW1476U89 structure (*19*). However, the electron density of the carbonyl group is well defined and is out of plane with the benzoyl ring in molecule 1 by −7.5° and −21.6° for the (10*R*)- and (10*S*)-diastereomers, respectively. A search of the Cambridge Structural Database with the *p*-aminobenzoic acid moiety revealed that deviations from planarity of the carbonyl with respect to the benzoyl ring of up ±40° are common. The binding site for this portion of the inhibitor is defined by residues Met 89, Ile 91, Leu 118, and Leu 143. The glutamate portion of the 10-formyl-TDAF exhibits the greatest flexibility as revealed by higher *B*-values. The side chain glutamate carboxylate forms a hydrogen bond with the main chain amide of Ile 91 and a salt bridge with Arg 64 (Table 4).

The most informative interactions concerning the mode of inhibition are in the formyl transfer region, surrounding the C10 position. The electron density maps show no connecting density that would suggest imine bond formation between the aldehyde carbon and the primary amine of the substrate, β-GAR (Figure 4), or any evidence for covalent attachment to an active site nucleophile. However, the density of the formyl transfer region can be interpreted as an equal occupancy for both the (10*R*)- and (10*S*)-diastereomers. Most interestingly, the electron density provided evidence that the aldehyde was actually bound as the hydrate. This hydrated aldehyde (gem-diol) provides not only a better fit to the electron density but also two additional hydrogen bonds with Asp 144 and His 108 that cannot be made by the aldehyde (Table 4 and Figure 6a).

The substrate, β-GAR, is tightly anchored in the binding groove at the phosphate group by several hydrogen bonds with the canonical phosphate binding loop connecting strand β1 and helix α1 of the N-terminal domain (Table 4). The phosphate region is much better defined compared to the rest of the substrate; however, the density around the anomeric carbon provides no evidence for binding of the α-anomer of the substrate that is present in the crystallization solution (Figure 4). The ribose ring of β-GAR was positioned in density taking into account hydrogen bond interactions from the O6 and O8 hydroxyl groups to the carboxylate side chain of Glu 173, as found in the 5-DATHF−β-GAR structure where the substrate appears to be well ordered from analysis of the *B*-values (Table 3). However, placement of the glycine portion of β-GAR was driven mainly by stereochemical restraints, due to poor electron density in this region (Figure 4). The presence of the inhibitor, 10-formyl-TDAF, is likely to have displaced the glycyl moiety of the substrate, and the glycine amine now makes a hydrogen bond to the main chain oxygen of Phe 88. It is interesting to note that despite the lack of imine bond formation between the inhibitor and substrate, crystallization studies have revealed evidence of bound 10-formyl-TDAF only in the presence of β-GAR. However, the kinetic data (*47*) do not provide any evidence for enhanced stability of the substrate−folate complex that would explain this observation. Thus, a combination of the pH-induced conformational changes that occur above pH 6.8 (*20*) and the possible differential solubility of the ternary complex (i.e., lower) versus the binary complex above pH 6.8 may enhance the formation of the ternary complex crystals. Consistent with that notion, we have not yet been able to obtain native crystals of *E. coli* GAR Tfase, or a binary complex with β-GAR above pH 6.8 [except for the E70A mutant protein (*20*)].

Superposition of the structure with that of the 5-DATHF−β-GAR complex shows that the primary amine of the β-GAR in the 5-DATHF−β-GAR complex is positioned very close to one of the hydroxyl groups of the hydrated aldehyde (Figure 6b). Thus, the structure adopted by the enzyme and 10-formyl-TDAF may actually provide a close mimic of the

Table 4: Hydrogen Bond Interactions (Å) between 10-Formyl-TDAF, β-GAR, and GAR Tfase

ligand atom	protein atom	molecule 1, *S* (Å)	molecule 1, *R* (Å)	molecule 2, *S* (Å)	molecule 2, *R* (Å)
10-formyl-TDAF					
NA	Leu 92 O	2.8	2.7	3.1	2.9
N3	Thr 140 O	2.7	2.9	2.7	2.8
O4	Asp 144 N	2.7	2.7	2.8	2.8
	Wat	3.1 (Wat 109)	3.2 (Wat 109)	3.3 (Wat 37)	3.3 (Wat 37)
N1	Leu 92 N	3.0	3.0	3.1	3.0
OE1	Ile 91 N	2.9	2.7	2.4	2.6
	Arg 64 $NH^{\epsilon 2}$	2.9	3.1	2.8	2.9
OE2	Arg 64 $NH^{\epsilon 1}$	2.9	3.2	–	–
	Glu 131 $O^{\epsilon 2}$ [a]	–	–	3.2	2.8
OA2	Asn 106-$N^{\delta 2}$	2.9	3.2	2.6	3.1
	Asp 144 $O^{\delta 1}$	2.4	2.6	2.7	3.5
	His 108 $N^{\delta 1}$	2.8	2.4	3.2	2.8
OA1	His 108 $N^{\delta 1}$	2.9	3.0	2.7	2.8
β-GAR					
O8	Ile 107 O	3.1		3.2	
	Glu 173 $O^{\epsilon 1}$	2.7		2.9	
O6	Glu 173 $O^{\epsilon 1}$	3.1		3.1	
	Glu 173 $O^{\epsilon 2}$	2.6		2.9	
O16	Wat	2.5 (Wat 13)		2.7 (Wat 117)	
	Asn 13 N	2.9		3.1	
	Wat	–		2.7 (Wat 119)	
	Asn 13 $N^{\delta 2}$	3.2		3.2	
O17	Ser 12 O^{γ}	2.9		2.9	
	Ser 12 N	2.6		2.5	
O18	Gly 11 N	2.8		3.0	
	Wat	2.9 (Wat 33)		2.7 (Wat 36)	
NH_2	Phe 88 O	3.0		2.6	

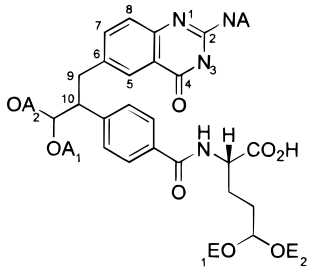

Hydrated 10-formyl-TDAF

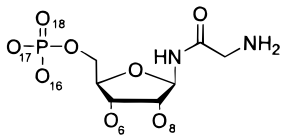

β-GAR

[a] Residue from a symmetry-related molecule 1.

transition state of the formyl transfer reaction (Figure 1), despite the fact that the 10 position of the inhibitor is different from that of the natural cofactor, 10-formyl-THF (sp^3 vs sp^2). Hence, the enhanced binding affinity of the inhibitor compared to the affinities of others prepared in this series (*21*, *23*, *24*) is derived from stabilizing hydrogen bond interactions within the enzyme active site in a manner that mimics the activation of formyl transfer.

^{13}C-Labeled 10-Formyl-TDAF and NMR Characterization of GAR Tfase Binding. To distinguish between the possibilities of bound diastereomers of the aldehyde or a bound aldehyde hydrate, a ^{13}C-labeled aldehyde was prepared and its binding to GAR Tfase was investigated by NMR. The final steps of the ^{13}C-labeled inhibitor synthesis were as previously described (*21*) with the exception being that the penultimate *N*,*N*-dimethylhydrazone cleavage to the sensitive aldehyde by ozonolysis, rather than buffered (pH 7.0) $CuCl_2$-promoted hydrolysis, provided a better (85 vs 46%) and more dependable conversion (Scheme 1). The ^{13}C-labeled *N*,*N*-dimethylhydrazone **6** was prepared from methyl 4-bromomethylbenzoate **1** with the economical K^{13}CN. A two-step selective reduction (*48*) of the nitrile in the presence of the methyl ester provided the ^{13}C-labeled aldehyde **5** and the immediate precursor to **6**.

In previous studies (*21*), 10-formyl-TDAF was shown to exist as a rapidly equilibrating diastereomeric mixture of aldehydes in aprotic solvents, but as a hydrated aldehyde (gem-diol) in water and a hemiacetal adduct in methanol, as was confirmed with the labeled inhibitor by ^{13}C NMR spectroscopy. 10-Formyl-TDAF exhibited only ^{13}C resonances of the diastereomeric aldehydes in the polar aprotic solvent DMSO-d_6, while only resonances that corresponded to the hydrate or hemiacetal were observed in D_2O, pH 7.5 phosphate buffer, or CD_3OD (Table 5). In the case of the hemiacetal formation in CD_3OD, each of the aldehyde diastereomers provides two diastereomeric hemiacetals that could be distinguished by ^{13}C NMR. These spectra and the corresponding behavior of the aldehyde confirmed its electrophilic character, provided diagnostic chemical shifts for both the aldehyde and hydrate forms of the inhibitor, and established the potential to distinguish either from β-GAR or enzyme-derived covalent adducts.

Initial attempts to examine the GAR Tfase bound inhibitor by ^{13}C NMR in the absence of the substrate β-GAR were

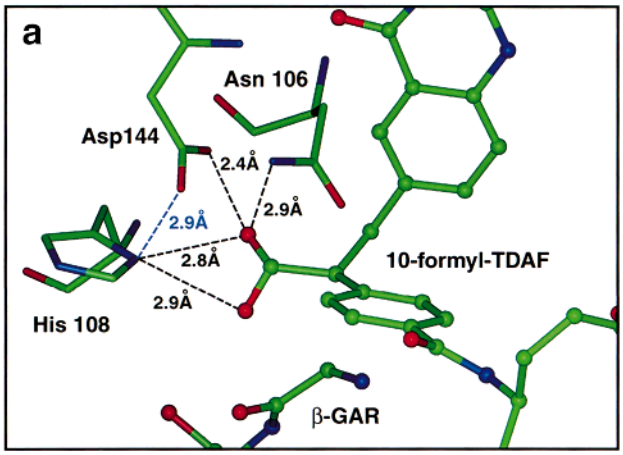

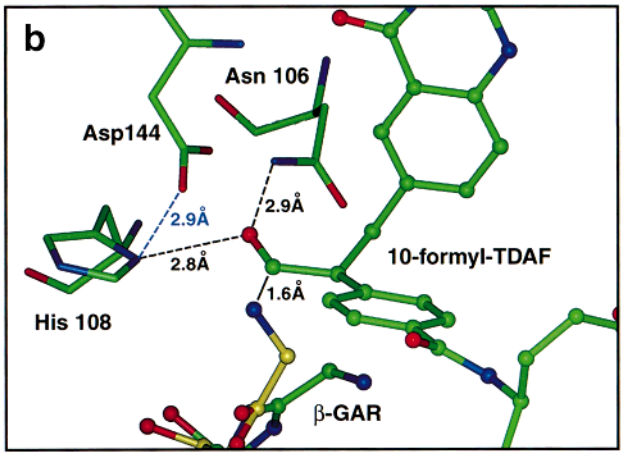

FIGURE 6: Hydrogen bond interactions between the inhibitor and the enzyme around the formyl transfer region. (a) Four hydrogen bonds are formed by the (10*S*)-hydrated aldehyde with the three catalytic residues as well as the salt bridge (blue) formed between Asp 144 and His 108. (b) Two hydrogen bonds that would exist in the (10*S*)-aldehyde and the position of the primary amine of β-GAR (yellow), as seen in the 5-DATHF−β-GAR ternary structure (Brookhaven PDB file 1CDE). The primary amine of β-GAR sits approximately where the second hydroxyl of the hydrated aldehyde is modeled and suggests that the structure observed in the hydrate form of 10-formyl-TDAF bound to *E. coli* GAR Tfase may mimic the proposed tetrahedral intermediate.

Table 5: ^{13}C Resonances of Labeled 10-Formyl-TDAF

solvent	^{13}C signals	form
DMSO-d_6	220.7, 220.6	aldehyde
pH 7.5 phosphate buffer	94.5, 94.4	hydrate
D_2O	94.2, 94.1	hydrate
CD_3OD	101.29, 101.24, 101.06, 100.99	hemiacetal

unsuccessful due to line broadening and the slow tumbling of the high-molecular weight enzyme. At 0.8 mM enzyme and 0.5−2.5 equiv of inhibitor, no observable ^{13}C NMR signal for the aldehyde or hydrate was detected even after 8 h (18 000 scans, 1 s PD, 90 °PW, broad band decoupling). Analogous results with ^{13}C-labeled inhibitor−protein complexes have been observed and discussed in detail (*49*−*51*). The more sensitive technique of ^{1}H−^{13}C heteronuclear multiple-quantum coherence spectroscopy (HMQC) (*45*, *52*) detected a clear cross-peak to the ^{13}C-attached proton. In pH

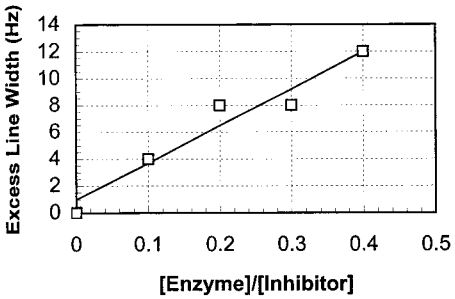

FIGURE 7: Plot of excess line width vs enzyme-to-inhibitor ratio for the ^{13}C-labeled 10-formyl-TDAF hydrate proton signal at δ 5.28 derived from the titration of inhibitor with enzyme in the absence of GAR.

7.5 phosphate buffer/D_2O, the two overlapping δ 93.6 and 5.28 (^{13}C−^{1}H) cross-peaks correspond to the hydrate form of the two aldehyde diastereomers and no cross-peak corresponding to the aldehyde form was detected (ca. δ 200 and 11−9). Titration of the ^{13}C-labeled 10-formyl-TDAF with GAR Tfase in the absence of the substrate β-GAR led to line broadening of the cross-peak that increased linearly (*49*) with enzyme concentration (Figure 7), which induced a small perturbation in its proton chemical shift (δ 5.28 → 5.26) without alteration of the ^{13}C chemical shift resonance (δ 93.6), and no detectable appearance of alternative cross-peaks diagnostic of either the aldehyde form of the inhibitor or an enzyme covalent adduct. The progressive line broadening and small chemical shift perturbation of the proton resonance, without the appearance of discrete signals for the bound and unbound inhibitor, indicate that they are in fast exchange. In addition, the small perturbation in the ^{1}H NMR chemical shift was upfield, further characteristic of the hydrate form, and not downfield, as would be required by averaging with a putative bound aldehyde. Thus, in the absence of the substrate β-GAR, the inhibitor binds noncovalently to the enzyme as the hydrate and is in fast exchange with the unbound inhibitor.

The analogous titration of the inhibitor with the enzyme was carried out in the presence of the substrate β-GAR. A small, but more pronounced, ^{1}H NMR upfield chemical shift (δ 5.28 → 5.24−5.20 and 5.09) without perturbation of the ^{13}C NMR chemical shift (δ 93.6−93.8) indicates a bound hydrate form of the inhibitor and excludes formation of a bound aldehyde, an enzyme covalent adduct, or a β-GAR imine or hemiaminal (Figure 8). Two cross-peaks for the hydrate were detected, one (δ 5.09) which is sharp and appears upon titration with enzyme, distinct from unbound inhibitor, and one which simply line broadens and slowly shifts with the enzyme titration from δ 5.28 to 5.24−5.20. These results have been assigned tentatively to the two bound hydrate diastereomers, one which is in slow exchange (δ 5.09) and the other in rapid exchange (δ 5.24−5.20). This interpretation suggests one of the hydrate diastereomers binds more tightly to the enzyme and, in the presence of the substrate β-GAR, forms a noncovalent complex that is temporally stable on the NMR time scale. This distinguishable behavior of the inhibitor in the presence or absence of β-GAR is consistent with the crystallization studies where bound inhibitor was observed only in the presence of β-GAR. However, due to the line broadening of the downfield signal at δ 5.24−5.20 and the accompanying loss of resolution, it is not clear whether this observation is due to a single

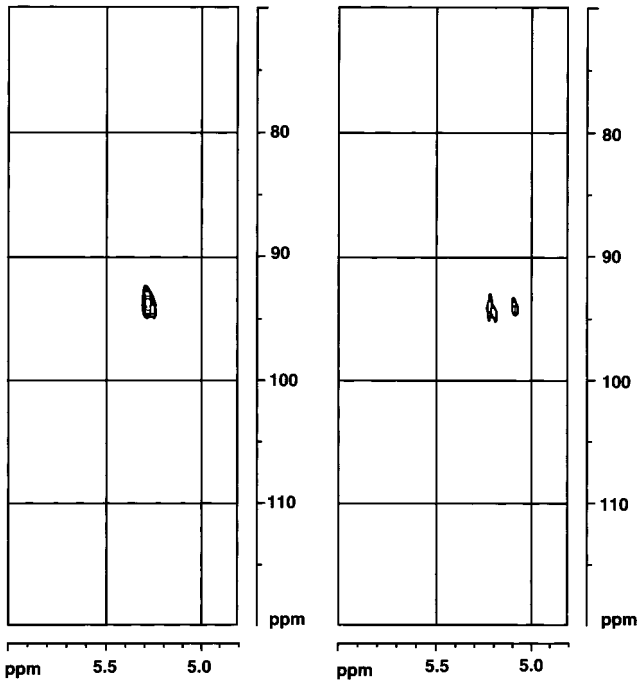

FIGURE 8: HMQC spectra of the ^{13}C-labeled 10-formyl-TDAF alone (left, 0.4 mM) and in the presence of substrate GAR and GAR Tfase (right; for GAR, a mixture of α- and β-isomers at 1.3 mM; for GAR Tfase, 0.64 mM).

resonance or multiple overlapping signals. Such overlapping signals might arise from multiple bound conformations of the inhibitor (i.e., the benzoylglutamate domain) or multiple bound conformational states of the enzyme (i.e., the disposition of the loop of residues 141−146).

Conclusion. The study with the ^{13}C-labeled 10-formyl-TDAF firmly established that both the free and bound inhibitor exist in the hydrate form, excluded the possibility of bound aldehyde, and further confirmed that a covalent adduct of the inhibitor with either the enzyme or the substrate β-GAR is not observed. Thus, this NMR study, combined with the interpretation of the electron density from the crystal structure, revealed that 10-formyl-TDAF binds as a hydrate mimic of the formyl transfer tetrahedral intermediate and, hence, permits a more detailed interpretation of the mechanism of inhibition. In the crystal structure, the formyl transfer region has well-defined electron density that identifies two hydrogen bonds that bridge the imidazole of His 108 to the oxygens of the hydrated aldehyde (Figure 6a). The bound hydrate benefits from direct hydrogen bonding to both Asp 144 and Asn 106, analogous to the interactions proposed to stabilize the protonated tetrahedral intermediate for the formyl transfer reaction (*19*, *20*). This structure, involving the bound hydrate, now beautifully explains the 10-fold difference in the inhibitor potency of 10-formyl-TDAF and the corresponding alcohol which lacks one of the two hydroxyl groups of the aldehyde hydrate and which, in turn, is approximately 10-fold more potent than inhibitors that lack the alcohol (*21*, *23*, *28*). Although it is premature to speculate on why 10-formyl-TDAF fails to form a GAR Tfase-assembled adduct with β-GAR, its geometry at the 10 position is different than that of the natural cofactor 10-formyl-THF (sp^3 vs sp^2). Due to the constraints of the folate and inhibitor core structures, this positions the formyl group in different orientations when bound at the GAR Tfase active site, potentially with 10-formyl-TDAF misaligned to react with GAR.

The discovery that 10-formyl-TDAF binds and inhibits GAR Tfase as a noncovalent hydrate (gem-diol) that acts as a mimic of the formyl transfer tetrahedral intermediate, analogous to the classical electrophilic aldehyde and ketone transition state inhibitors of proteases, provides novel design strategies for a future generation of new inhibitors for GAR Tfase. To date, this analogy between the folate-dependent formyl transfer reactions and peptide protease or transaminase reactions has not been recognized or exploited for the development of inhibitors.

ACKNOWLEDGMENT

We thank the staff of Stanford Synchrotron Radiation Laboratory (SSRL) beam line 9-1 for helpful support and Nancy-Ellen Haynes for preliminary supplies of 10-formyl-5,8,10-TDAF, and we are especially grateful to Dr. D. Huang and Dr. L. Pasternack for their assistance in securing the ^{1}H−^{13}C HMQC spectra of GAR Tfase-bound [^{13}C]-10-formyl-TDAF. This is publication 12598-MB from the Scripps Research Institute.

REFERENCES

1. Dev, I. K., and Harvey, R. J. (1978) *J. Biol. Chem. 253*, 4242−4244.
2. Inglese, J., Johnson, D. L., and Benkovic, S. J. (1986) in *Chemistry and Biology of Pteridines* (Curtius, H. C., Ghisla, N., and Blan, N., Eds.) pp 951−956, de Gruyter, Berlin.
3. Inglese, J., Johnson, D. L., Shiau, A., Smith, J. M., and Benkovic, S. J. (1990) *Biochemistry 29*, 1436−1443.
4. Davies, J. F. D., Delcamp, T. J., Prendergast, N. J., Ashford, V. A., Freisheim, J. H., and Kraut, J. (1990) *Biochemistry 29*, 9467−9479.
5. Oefner, C., D'Arcy, A., and Winkler, F. K. (1988) *Eur. J. Biochem. 174*, 377−385.
6. Montfort, W. R., Perry, K. M., Fauman, E. B., Finer-Moore, J. S., Maley, G. F., Hardy, L., Maley, F., and Stroud, R. M. (1990) *Biochemistry 29*, 6964−6977.
7. Hardy, L. W., Finer-Moore, J. S., Montfort, W. R., Jones, M. O., Santi, D. V., and Stroud, R. M. (1987) *Science 235*, 448−455.
8. Kamen, B. (1997) *Semin. Oncol. 24* (Suppl. 18), 30−39.
9. Takimoto, C. H. (1997) *Semin. Oncol. 24* (Suppl. 18), 40−51.
10. Beardsley, G. P., Moroson, B. A., Taylor, E. C., and Moran, R. G. (1989) *J. Biol. Chem. 264*, 328−333.
11. Mendelsohn, L. G., Shih, C., Schultz, R. M., and Worzella, J. F. (1996) *Invest. New Drugs 14*, 287−294.
12. Jackson, R. C., and Harkrader, R. J. (1981) in *Nucleosides and Cancer Treatment* (Tattersall, M. H. N., and Fox, R. M., Eds.) pp 18−31, Academic Press, Sydney.
13. Erba, E., Sen, S., Sessa, C., Vikhanskaya, F. L., and D'Incalci, M. (1994) *Br. J. Cancer 69*, 205−211.
14. Habeck, L. L., Leitner, T. A., Shackelford, K. A., Gossett, L. S., Schultz, R. M., Andis, S. L., Shih, C., Grindey, G. B., and Mendelsohn, L. G. (1994) *Cancer Res. 54*, 1021−1026.
15. Boritzki, T. J., Barlett, C. A., Zhang, C., and Howland, E. F. (1996) *Invest. New Drugs 14*, 295−303.
16. Faessel, H. M., Slocum, H. K., Jackson, R. C., Boritzki, T. J., Rustum, Y. M., Nair, M. G., and Greco, W. R. (1998) *Cancer Res. 58*, 3036−3050.
17. Chen, P., Schulze-Gahmen, U., Stura, E. A., Inglese, J., Johnson, D. L., Marolewski, A., Benkovic, S. J., and Wilson, I. A. (1992) *J. Mol. Biol. 227*, 283−292.
18. Almassy, R. J., Janson, C. A., Kan, C. C., and Hostomska, Z. (1992) *Proc. Natl. Acad. Sci. U.S.A. 89*, 6114−6118.

19. Klein, C., Chen, P., Arevalo, J. H., Stura, E. A., Marolewski, A., Warren, M. S., Benkovic, S. J., and Wilson, I. A. (1995) *J. Mol. Biol. 249*, 153−175.
20. Su, Y., Yamashita, M. M., Greasley, S. E., Mullen, C. A., Jennings, P. A., Warren, M. S., Benkovic, S. J., and Wilson, I. A. (1998) *J. Mol. Biol. 281*, 485−499.
21. Boger, D. L., Haynes, N. E., Kitos, P. A., Warren, M. S., Ramcharan, J., Marolewski, A. E., and Benkovic, S. J. (1997) *Bioorg. Med. Chem. 5*, 1817−1830.
22. Smith, G. K., Mueller, W. T., Benkovic, P. A., and Benkovic, S. J. (1981) *Biochemistry 20*, 1241−1245.
23. Boger, D. L., Haynes, N. E., Warren, M. S., Gooljarsingh, L. T., Ramcharan, J., Kitos, P. A., and Benkovic, S. J. (1997) *Bioorg. Med. Chem. 5*, 1831−1838.
24. Boger, D. L., Haynes, N. E., Warren, M. S., Ramcharan, J., Kitos, P. A., and Benkovic, S. J. (1997) *Bioorg. Med. Chem. 5*, 1839−1846.
25. Boger, D. L., Haynes, N. E., Warren, M. S., Ramcharan, J., Kitos, P. A., and Benkovic, S. J. (1997) *Bioorg. Med. Chem. 5*, 1853−1857.
26. Caperelli, C. A., and Conigliaro, J. (1986) *J. Med. Chem. 29*, 2117−2119.
27. Caperelli, C. A. (1987) *J. Med. Chem. 30*, 1254−1256.
28. Boger, D. L., Haynes, N. E., Warren, M. S., Ramcharan, J., Marolewski, A. E., Kitos, P. A., and Benkovic, S. J. (1997) *Bioorg. Med. Chem. 5*, 1847−1852.
29. Inglese, J., Blatchly, R. A., and Benkovic, S. J. (1989) *J. Med. Chem. 32*, 937−940.
30. Ducruix, A., and Giege, R. (1992) *Crystallization of Nucleic Acids and Proteins: A Practical Approach*, Oxford University Press, New York.
31. Hope, H. (1988) *Acta Crystallogr. B44*, 22−26.
32. Otwinowski, Z., and Minor, W. (1997) *Methods Enzymol. 276*, 307−326.
33. Matthews, B. W. (1968) *J. Mol. Biol. 33*, 491−497.
34. Navaza, J. (1994) *Acta Crystallogr. A50*, 157−163.
35. Collaborative Computational Project 4 (1994) *Acta Crystallogr. D50*, 760−763.
36. Brünger, A. T. (1992) *X-PLOR*, version 3.1, Yale University Press, New Haven, CT.
37. Brünger, A. T. (1992) *Nature 355*, 472−475.
38. Jones, T. A., Zou, J. Y., Cowan, S. W., and Kjeldgaard, M. (1991) *Acta Crystallogr. A47*, 110−119.
39. Caperelli, C. A., and Price, M. F. (1988) *Arch. Biochem. Biophys. 264*, 340−342.
40. Antle, V. D., Liu, D., McKellars, B. R., Caperelli, C. A., Hua, M., and Vince, R. (1996) *J. Biol. Chem. 271*, 6045−6049.
41. Klegwegt, G. J. (1995) *CCP4/ESF-EACBM Newsletter on Protein Crystallography*, 45−50.
42. Jiang, J. S., and Brünger, A. T. (1994) *J. Mol. Biol. 243*, 100−115.
43. Brünger, A. T., Adams, P. D., Clore, G. M., DeLano, W. L., Gros, P., Grosse-Kunstleve, R. W., Jiang, J. S., Kuszewski, J., Nilges, M., Pannu, N. S., Read, R. J., Rice, L. M., Simonson, T., and Warren, G. L. (1998) *Acta Crystallogr. D54*, 905−921.
44. Laskowski, R. A., MacArthur, M. W., Moss, D. S., and Thornton, J. M. (1993) *J. Appl. Crystallogr. 26*, 283−291.
45. Summers, M. F., Marzilli, L., and Bax, A. (1986) *J. Am. Chem. Soc. 108*, 4285−4294.
46. Warren, M. S., Marolewski, A. E., and Benkovic, S. J. (1996) *Biochemistry 35*, 8855−8862.
47. Shim, J. H., and Benkovic, S. J. (1998) *Biochemistry 37*, 8776−8782.
48. Meyers, A. I., Nabeya, A., Adickers, H. W., Politzer, I. R., Malone, G. R., Kovelesky, A. C., Nolen, R. L., and Portnoy, R. C. (1973) *J. Org. Chem. 38*, 36−56.
49. Gorenstein, D. G., Kar, D., and Momii, R. K. (1976) *Biochem. Biophys. Res. Commun. 73*, 105−111.
50. Kahyaoglu, A., Haghjoo, K., Kraicsovits, F. J., and Polgar, L. (1997) *Biochem. J. 322*, 839−843.
51. Wang, X., and Goff, H. M. (1997) *Biochim. Biophys. Acta 1339*, 88−96.
52. Malcolm, B. A., Lowe, C., Shechosky, S., McKay, R. T., Yang, C. C., Shah, V. J., Simon, R. J., Vederas, J. C., and Santi, D. V. (1995) *Biochemistry 34*, 8172−8179.

BI991888A